Langmuir Article

pubs.acs.org/Langmuir

Electric-Field-Induced Interfacial Instabilities and Morphologies of Thin Viscous and Elastic Bilayers

Dipankar Bandyopadhyay,[†] Ashutosh Sharma,*[,†] Uwe Thiele,[‡] and P. Dinesh Sankar Reddy[†]

[†]*Department of Chemical Engineering, Indian Institute of Technology, Kanpur 208016, India, and* [‡]*Department of Mathematical Sciences, Loughborough University, Leicestershire LE11 3TU, UK*

Received February 21, 2009. Revised Manuscript Received April 4, 2009

Electric-field-induced instabilities in thin bilayers composed of either purely viscous or purely elastic films resting on a solid substrate are studied. In contrast to the electric-field-induced instability in a single elastic film, the length scale of the instability for elastic bilayers can be tuned by changing the ratios of the shear moduli, thicknesses, and dielectric permittivities of the films. Linear stability analysis is employed to uncover the variations in the wavelength. The instabilities of the viscous bilayers follow different modes of interfacial evolution: either in-phase *bending* or antiphase *squeezing*. Linear and nonlinear analyses show that the mode type can be switched by changing the dielectric permittivities of the films. Nonlinear simulations find a number of intriguing interfacial morphologies: (a) an embedded upper layer in an array of lower layer columns, (b) upper layer columns encapsulated by lower layer beakers, (c) lower layer columns covered by the upper layer liquid resulting in concentric core−shell columns, (d) droplets of upper liquid on a largely undisturbed lower layer, and (f) evolution of two different wavelengths at the two interfaces of the bilayer. The simulated morphology types (a), (b) and (d) have been seen previously in experiments.[39,41,45] The effect of the film viscosities on the evolution of the instability and final morphologies is also discussed.

I. Introduction

Self-organized surface patterns of thin (< 100 nm) polymer films have recently been studied extensively because of their technological and scientific importance.[1−24] The instabilities engendered by intermolecular interactions or by externally applied fields are often employed to generate patterns. Recent studies on the patterning[25−28] of polymer films have also been motivated by technological applications in soft lithography, microfabricated integrated circuits, DNA arrays,[26] biological optics for advanced photonic systems,[27] microfluidics,[28] and so forth. Understanding the stability, dynamics, and morphology of polymer films is also important because such systems appear in various products and processes ranging from coatings, adhesives, flotation, and biological membranes to a host of areas in nanotechnology. Thin polymer films are also model mesoscale systems for the study of several fundamental scientific issues such as deformations in biological membranes,[29,30] intermolecular forces, self-organization of interfaces, confinement and finite-size effects, mesoscale dewetting, multilayer adsorption, and phase transitions. This motivates the continuous research effort aimed at understanding the instabilities and the dynamics of thin polymer films.

*Author to whom correspondence should be addressed. E-mail: ashutos@iitk.ac.in.

(1) Ruckenstein, E.; Jain, R. K. *J. Chem. Soc., Faraday Trans. 2* 1974, *70*, 132.
(2) De Gennes, P. G. *Rev. Mod. Phys.* **1985**, *57*, 827.
(3) Brochard-Wyart, F.; Daillant, J. *Can. J. Phys.* **1990**, *68*, 1084.
(4) Brochard-Wyart, F.; Martin, P.; Redon, C. *Langmuir* **1993**, *9*, 3682.
(5) Sharma, A. *Langmuir* **1993**, *9*, 861.
(6) Sharma, A.; Jameel, A. T. *J. Colloid Interface Sci.* **1993**, *161*, 190.
(7) Oron, A.; Davis, S. H.; Bankoff, S. G. *Rev. Mod. Phys.* **1997**, *69* 931.
(8) Sharma, A.; Khanna, R. *Phys. Rev. Lett.* **1998**, *81*, 3463.
(9) Herminghaus, S.; Jacobs, K.; Mecke, K.; Bischof, J.; Fery, A.; Ibn-Elhaj, M.; Schlagowski, S. *Science* **1998**, *282*, 916.
(10) Ghatak, A.; Khanna, R.; Sharma, A. *J. Colloid Interface Sci.* **1999**, *212*, 483.
(11) Yerushalmi-Rozen, R.; Kerle, T.; Klein, J. *Science* **1999**, *285* 1254.
(12) Oron, A.; Bankoff, S. G. *J. Colloid Interface Sci.* **1999**, *218* 152.
(13) Thiele, U.; Velarde, M. G.; Neuffer, K. *Phys. Rev. Lett.* **2001**, *87* 016104.
(14) Konnur, R.; Kargupta, K.; Sharma, A. *Phys. Rev. Lett.* **2000**, *84*, 931.
(15) Kargupta, K.; Sharma, A. *Phys. Rev. Lett.* **2001**, *86*, 4536.
(16) Brinkmann, M.; Lipowsky, R. *J. Appl. Phys.* **2002**, *92*, 4296.
(17) Brusch, L.; Kühne, H.; Thiele, U.; Bär, M. *Phys. Rev. E* **2002**, *66* 011602.
(18) Thiele, U.; Brusch, L.; Bestehorn, M.; Bär, M. *Eur. Phys. J. E.* **2003**, *11*, 255.
(19) Becker, J.; Grün, G.; Seemann, R.; Mantz, H.; Jacobs, K.; Mecke, K. R.; Blossey, R. *Nat. Mater.* **2003**, *2*, 59.
(20) Kao, J. C. T.; Golovin, A. A.; Davis, S. H. *J. Colloid Interface Sci.* **2006**, *303*, 532.
(21) Simmons, D.; Chauhan, A. *J. Colloid Interface Sci.* **2006**, *295* 472.
(22) Saprykin, S.; Trevelyan, P. M. J.; Koopmans, R. J.; Kalliadasis, S. *Phys. Rev. E.* **2007**, *75*, 026306.
(23) Volodin, P.; Kondyurin, A. *J. Phys. D: Appl. Phys.* **2008**, *41* 065306.
(24) Simmons, D.; Chauhan, A. *J. Colloid Interface Sci.* **2006**, *269*, 35.
(25) Zhihong, N.; Kumacheva, E. *Nat. Mater.* **2008**, *7*, 277.
(26) Langer, R.; Tirrell, D. A. *Nature* **2004**, *428*, 487.
(27) Lee, L. P.; Szema, R. *Science* **2005**, *310*, 1148.
(28) Squires, T. M.; Quake, S. R. *Rev. Mod. Phys.* **2005**, *77*, 977.
(29) de Souza, E. R.; Gallez, D. *Phys. Fluids* **1998**, *10*, 1804.
(30) Coakley, W. T.; Gallez, D.; de Souza, E. R.; Gauci, H. *Biophys. J.* **1990**, *77*, 817.

Previous studies[31−61] reveal that the application of an external electric field is a simple and versatile method to generate self-organized mesoscale polymer patterns on solid substrates. Experimental works[35−49] show that the application of an electric field across initially flat interfaces of ultrathin polymer films may lead to the formation of regular, hierarchical[39] and phase inverted[45] columnar structures. It is well understood[31−34] that, above a critical field strength, the electric-field-induced instabilities at macroscopic fluid interfaces lead to the growth of intermediate wave numbers because gravity and capillary forces stabilize long and short wavelength disturbances, respectively. The studies involving the electric-field-induced deformation of elastic films under air demonstrate that the surface of thin elastic films can also deform into complex interfacial patterns when an applied electric field overcomes the restoring elastic and capillary forces.[49,61] Thus far, the characteristics of the electric-field-induced instabilities have been studied for (i) a thin dielectric film in air,[35,36,38,43,44,46−48,51,57−59] (ii) a bilayer of a dielectric and a conducting fluid,[52] (iii) a bilayer of viscous dielectric liquids,[37,40] (iv) a single layer of leaky dielectric liquid with an air gap above,[50] (v) a bilayer of leaky dielectric liquids,[53−56] (v) a bilayer of viscous liquids under air,[39,41,45,60] and (vi) a single elastic film under air.[61]

Figure 1 shows a schematic diagram of a bilayer. The interfacial dynamics of bilayers involves the coupled deformations of the two interfaces. The presence of twin fluid interfaces allows for two basic modes of surface instabilities:[62] either in-phase *bending* or antiphase *squeezing*. A number of experimental[63−73] and theoretical[74−90] works show many interesting features of viscous and viscoelastic bilayer dynamics under the influence of van der Waals forces. Recent studies[71,90] of the patterning of elastic bilayers under the influence of van der Waals forces show that the length scale of the patterns do not only vary with the film thickness but also depend on the physical properties of the films. However, the use of an external electric field allows for a better control of the destabilizing forces because the field strength can be easily modulated. Only few experimental[39,41,45] and theoretical[60] works focus on the bilayer instabilities under the influence of an external electric field.

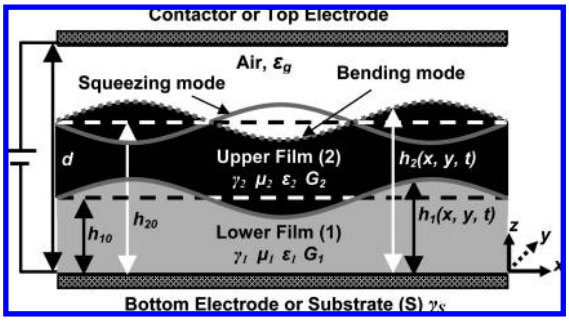

Figure 1. A schematic diagram of a bilayer under the influence of a static electric field applied through the electrodes, (i) the solid substrate on which the bilayer rests, and (ii) the contactor that is placed at the top. The mean and the local thicknesses of the lower [composite] layer are h_{10} and h_1 (x,y,t) [h_{20} and h_2 (x,y,t)], respectively. The material parameters γ_1, γ_2, and γ_s are the surface energies of the lower layer, the upper layer and the solid substrate, ε_1, ε_2, and ε_g are the relative dielectric constants of the lower layer, upper layer and air, μ_2 and μ_1 denote the viscosities of the upper and lower layer, G_2 and G_1 denote the shear modulus of the upper and lower layer, and d is the distance between the electrodes. The solid and the dotted line at the upper interface indicate the *squeezing* and *bending* modes of evolution with respect to the solid line at the lower interface. The dashed horizontal lines indicate the base state.

(31) Swan, J. W. *Proc. R. Soc. London* **1897**, *62*, 38.
(32) Taylor, G. I.; McEwan, A. D. *J. Fluid Mech.* **1965**, *1*, 22.
(33) Melcher, J. R.; Smith, C. V. *Phys. Fluids* **1969**, *12*, 778.
(34) Saville, D. A. *Annu. Rev. Fluid Mech.* **1997**, *29*, 27.
(35) Schäffer, E.; Thurn-Albrecht, T.; Russell, T. P.; Steiner, U. *Nature (London)* **2000**, *403*, 874.
(36) Schäffer, E.; Thurn-Albrecht, T.; Russell, T. P.; Steiner, U. *Europhys. Lett.* **2001**, *53*, 518.
(37) Lin, Z.; Kerle, T.; Baker, S. M.; Hoagland, D. A.; Schaffer, E.; Steiner, U.; Russell, T. P. *J. Chem. Phys.* **2001**, *114*, 2377.
(38) Deshpande, P.; Sun, X.; Chou, S. Y. *Appl. Phys. Lett.* **2001**, *79*, 1688.
(39) Morariu, M. D.; Voicu, N. E.; Schäffer, E.; Lin, Z.; Russell, T. P.; Steiner, U. *Nat. Mater.* **2003**, *2*, 48.
(40) Lin, Z. Q.; Kerle, T.; Russell, T. P.; Schäffer, E.; Steiner, U. *Macromolecules* **2002**, *35*, 3971.
(41) Lin, Z. Q.; Kerle, T.; Russell, T. P.; Schäffer, E.; Steiner, U. *Macromolecules* **2002**, *35*, 6255.
(42) Xu, T.; Hawker, C. J.; Russell, T. P. *Macromolecules* **2003**, *36*, 6178.
(43) Xiang, H.; Lin, Y.; Russell, T. P. *Macromolecules* **2004**, *37*, 5358.
(44) Leach, K. A.; Lin, Z.; Russell, T. P. *Macromolecules* **2005**, *38*, 4868.
(45) Leach, K. A.; Gupta, S.; Dickey, M. D.; Wilson, C. G.; Russell, T. P. *Chaos* **2005**, *15*, 047506.
(46) Harkema, S.; Steiner, U. *Adv. Funct. Mater.* **2005**, *15*, 2016.
(47) Wu, N.; Pease, L. F.III; Russel, W. B. *Adv. Funct. Mater.* **2006**, *16*, 1992.
(48) Voicu, N. E.; Harkema, S.; Steiner, U. *Adv. Func. Mater.* **2006**, *16*, 926.
(49) Arun, N.; Sharma, A.; Shenoy, V.; Narayan, K. S. *Adv. Mater.* **2006**, *18*, 660.
(50) Tomar, G.; Shankar, V.; Sharma, A.; Biswas, G. *J. Non-Newtonian Fluid Mech.* **2007**, *143*, 120.
(51) Tseluiko, D.; Blyth, M. G.; Papageorgiou, D. T.; Vanden-Broeck, J.-M. *J. Fluid Mech.* **2008**, *597*, 449.
(52) Herminghaus, S. *Phys. Rev. Lett.* **1999**, *83*, 2359.
(53) Pease, L. F.III; Russel, W. B. *J. Chem. Phys.* **2003**, *118*, 3790.
(54) Pease, L. F.III; Russel, W. B. *Langmuir* **2005**, *21*, 12290.
(55) Shankar, V.; Sharma, A. *J. Colloid Interface Sci.* **2004**, *274*, 294.
(56) Craster, R. V.; Matar, O. K. *Phys. Fluids.* **2005**, *17*, 032104.
(57) Verma, R.; Sharma, A.; Kargupta, K.; Bhaumik, J. *Langmuir* **2005**, *21*, 3710.
(58) John, K.; Thiele, U. *Appl. Phys. Lett.* **2007**, *90*, 264102.
(59) John, K.; Hänggi, P.; Thiele, U. *Soft Matter* **2008**, *4*, 1183.
(60) Bandyopadhyay, D.; Sharma, A. *J. Colloid Interface Sci.* **2007**, *311*, 595.
(61) Sarkar, J.; Sharma, A.; Shenoy, V. *Phys. Rev. E.* **2008**, *77*, 031604.
(62) Maldarelli, C. H.; Jain, R. K.; Ivanov, I. B.; Ruckenstein, E. *J. Colloid Interface Sci.* **1980**, *78*, 118.
(63) Higgins, A. M.; Jones, R. A. L. *Nature* **2000**, *404*, 476.
(64) Lambooy, P.; Phelan, K. C.; Haugg, O.; Krausch, G. *Phys. Rev. Lett.* **1996**, *76*, 1110.
(65) Pan, Q.; Winey, I. K.; Hu, H. H.; Composto, R. J. *Langmuir* **1997**, *13*, 1758.
(66) Segalman, R. A.; Green, P. F. *Macromolecules* **1999**, *32*, 801.
(67) Wang, C.; Krausch, G.; Geoghegan, M. *Langmuir* **2001**, *17*, 6269.
(68) Kang, H.; Lee, S. H.; Kim, S.; Char, K. *Macromolecules* **2003**, *36*, 8579.
(69) Wunnicke, O.; Müller-Buschbaum, P.; Wolkenhauer, M.; Lorenz-Haas, C.; Cubitt, R.; Leiner, V.; Stamm, M. *Langmuir* **2003**, *19*, 8511.
(70) Julien LeOpolde, S.; Damman, P. *Nat. Mater.* **2006**, *5*, 957.
(71) Mukherjee, R.; Pangule, R.; Sharma, A.; Gaurav, T. *Adv. Funct. Mater.* **2007**, *17*, 2356.
(72) de Silva, J. P.; Geoghegan, M.; Higgins, A. M.; Krausch, G.; David, M. O.; Reiter, G. *Phys. Rev. Lett.* **2007**, *98*, 267802.
(73) Paul, R.; Karabiyik, U.; Swift, M. C.; Hottle, J. R.; Esker, A. R. *Langmuir* **2008**, *24*, 4676.
(74) Danov, K. D.; Paunov, V. N.; Alleborn, N.; Raszillier, H.; Durst, F. *Chem. Eng. Sci.* **1998**, *53*, 2809.
(75) Danov, K. D.; Paunov, V. N.; Stoyanov, S. D.; Alleborn, N.; Raszillier, H.; Durst, F. *Chem. Eng. Sci.* **1998**, *53*, 2823.
(76) Paunov, V. N.; Danov, K. D.; Alleborn, N.; Raszillier, H.; Durst, F. *Chem. Eng. Sci.* **1998**, *53*, 2839.
(77) Pototsky, A.; Bestehorn, M.; Merkt, D.; Thiele, U. *Phys. Rev. E* **2004**, *70*, 025201.
(78) Bandyopadhyay, D.; Gulabani, R.; Sharma, A. *Ind. Eng. Chem. Res.* **2005**, *44*, 1259.
(79) Pototsky, A.; Bestehorn, M.; Merkt, D.; Thiele, U. *J. Chem. Phys.* **2005**, *122*, 224711.
(80) Fisher, L. S.; Golovin, A. A. *J. Colloid Interface Sci.* **2005**, *291*, 515.
(81) Bandyopadhyay, D.; Sharma, A. *J. Chem. Phys.* **2006**, *125*, 054711.
(82) Pototsky, A.; Bestehorn, M.; Merkt, D.; Thiele, U. *Europhys. Lett.* **2006**, *74*, 665.
(83) Bandyopadhyay, D.; Sharma, A. *J. Phys. Chem. B* **2008**, *112*, 11564.
(84) Nepomnyashchy, A. A.; Simanovskii, I. B. *Phys. Fluids* **2006**, *18*, 112101.
(85) Nepomnyashchy, A. A.; Simanovskii, I. B. *Phys. Fluids* **2006**, *18*, 032105.
(86) Kumar, S.; Matar, O. K. *J. Colloid Interface Sci.* **2004**, *273*, 581.
(87) Matar, O. K.; Gkanis, V.; Kumar, S. *J. Colloid Interface Sci.* **2005**, *286*, 319.
(88) Fisher, L. S.; Golovin, A. A. *J. Colloid Interface Sci.* **2007**, *307*, 203.
(89) Lenz, R. D.; Kumar, S. *J. Colloid Interface Sci.* **2007**, *316*, 660.
(90) Tomar, G.; Sharma, A.; Shenoy, V.; Biswas, G. *Phys. Rev. E.* **2007**, *76*, 011607.

In the present work, we study the stability, dynamics, and morphology of either purely elastic or purely viscous bilayers subjected to an external electric field. Linear stability analysis (LSA) shows that in both cases, the physical properties (shear modulus, viscosity, and dielectric permittivity) and thicknesses of the films can profoundly influence the length and time scales of the evolving structures. In a previous study,[60] we focused on the short-time linear and two-dimensional (2-D) nonlinear analyses for a viscous bilayer. The true morphology and pattern formation cannot be captured by 2-D simulations. For example, the effects of out-of-plane curvature and flow are not retained in two dimensions. In this study, we consider the electric-field-induced instabilities of both viscous and elastic bilayers, including the study of the long-time evolution in three dimensions (3-D). Further, we extend the analysis of a previous study on purely viscous bilayers,[60] where a simplified, but incomplete electrical potential was considered at the liquid−liquid interface. Finally, we compare the simulated interfacial morphologies with those observed in recent experiments.[39,41,45]

II. Problem Formulation

In this section, we formulate the governing equations for an elastic bilayer under the influence of a destabilizing electric field and develop a linear theory to study the length and time scales of interfacial instabilities in such systems. Following this, long-wave linear and nonlinear analyses of a thin viscous bilayer are presented.

In what follows, x and y are the span-wise and transverse coordinates parallel to the substrate, respectively, and z is the coordinate normal to the substrate (as shown in Figure 1). The symbol t represents time, the subscript i denotes the respective layer ($i = 1$ lower layer and $i = 2$ upper layer, $i = s$ denotes solid substrate and $i = g$ denotes bounding nonviscous gas). The superscripts denote components of vectors. Thus, for the layer i, u_i^x and u_i^z are the x- and z-components of displacement, v_i^x, v_i^y, and v_i^z are the x-, y-, and z-components of velocity, G_i is the shear modulus, μ_i is the viscosity, ρ_i is the density, γ_i is the surface tension, ε_i is the dielectric permittivity, π_i is the excess pressure due to the externally applied electric field, $P_i = p_i - \pi_i$ is the effective, nonbody force pressure inside the films, and p_i denotes the isotropic static pressure in the liquid. The subscripts t, x, y, and z denote differentiation with respect to time and the respective coordinate. The variable thicknesses of the bilayer and of the lower layer are represented by h_2 and h_1, respectively. Thus, $h_3 = h_2 - h_1$ is the thickness of the upper layer. The symbols h_{20}, h_{10}, and h_{30} represent the respective constant base state thicknesses.

1. Elastic Bilayer. *A. Governing Equations.* Inertia is neglected from the equations of motion owing to the small thicknesses of the elastic films. In consequence, the equations of motion and the condition for incompressibility that describe the deformations of the elastic layers are

$$-\nabla P_i + \nabla\cdot\sigma_i = 0 \quad \text{and} \quad \nabla\cdot\mathbf{u}_i = 0 \tag{1}$$

Here $\boldsymbol{\sigma}_i[= G_i(\nabla\mathbf{u}_i + \nabla\mathbf{u}_i^T)]$ is the stress tensor and $\mathbf{u}_i\{u_i^x, u_i^z\}$ is the displacement vector of the ith layer.

B. Boundary Conditions. At $z = 0$, no-slip and impermeability boundary conditions ($\mathbf{u}_1 = 0$) are applied. At $z = h_1$, continuity of x- and z-components of displacements ($\mathbf{u}_1 = \mathbf{u}_2$), shear stress balance ($\mathbf{t}_1\cdot\boldsymbol{\sigma}_2\cdot\mathbf{n}_1 = \mathbf{t}_1\cdot\boldsymbol{\sigma}_1\cdot\mathbf{n}_1$), normal stress balance ($\mathbf{n}_1\cdot\boldsymbol{\sigma}_2\cdot\mathbf{n}_1 - \mathbf{n}_1\cdot\boldsymbol{\sigma}_1\cdot\mathbf{n}_1 = \gamma_{21}\kappa_1$), and the kinematic condition ($\dot{h}_1 + (\dot{\mathbf{u}}_1\cdot\nabla_s)h_1 = \dot{\mathbf{u}}_1\cdot\mathbf{n}_1$) are enforced. At $z = h_2$, the normal stress balance ($\mathbf{n}_2\cdot\boldsymbol{\sigma}_2\cdot\mathbf{n}_2 = -\gamma_2\kappa_2$), shear stress balance ($\mathbf{t}_2\cdot\boldsymbol{\sigma}_2\cdot\mathbf{n}_2 = 0$) and the kinematic condition ($\dot{h}_2 + (\dot{\mathbf{u}}_2\cdot\nabla_s)h_2 = \dot{\mathbf{u}}_2\cdot\mathbf{n}_2$) are enforced. Here $\mathbf{n}_i$ and $\mathbf{t}_i$ are normal and tangent vectors, and ∇_s is the surface gradient operator at the interfaces. The superscript dot in the expressions represents the time derivative of the variables.

C. Excess Pressure Engendered by Electric Field. The excess pressure at the interfaces π_1 and π_2 resulting from the electric field can be obtained by considering the substrate and the contactor in Figure 1 as two electrodes. They attract each other because of their opposite charges when the electric field is turned on. The electric field polarizes the dielectric polymers resulting in an effective surface charge density and hence in an excess pressure at the deformable polymer interfaces. The capacitance of the composite layer (C) can be expressed as for a series capacitor:

$$\frac{1}{C} = \frac{1}{C_1} + \frac{1}{C_2} + \frac{1}{C_g}, \text{ where } C_1 = \frac{\varepsilon_0\varepsilon_1\overline{A}}{h_1}, \quad C_2 = \frac{\varepsilon_0\varepsilon_2\overline{A}}{(h_2 - h_1)}, \text{ and } C_g = \frac{\varepsilon_0\overline{A}}{(d - h_2)} \tag{2}$$

Here C_1, C_2, and C_g represent the capacitances of the lower layer, upper layer, and bounding medium, respectively, $\overline{A}$ represents the area of the flat interfaces, and d is the distance between the electrodes. For a constant voltage ψ, the free energy stored in the capacitor device is

$$\Delta G = -\frac{1}{2}C\psi^2 = \frac{\varepsilon_0\varepsilon_1\varepsilon_2\psi^2}{2}\left[\frac{1}{[(h_1 + h_3)\varepsilon_1[\varepsilon_2 - 1] - h_1[\varepsilon_2 - \varepsilon_1] - \varepsilon_2\varepsilon_1 d]}\right] \tag{3}$$

The excess pressures at the interfaces π_1 and π_2 correspond to derivatives of eq 3 with respect to the respective layer thickness:

$$\pi_1 = \frac{\partial(-\Delta G)}{\partial h_1} = -\left[\frac{\varepsilon_0\varepsilon_1\varepsilon_2\psi^2([\varepsilon_2 - \varepsilon_1] + \varepsilon_1[1 - \varepsilon_2])}{2[\varepsilon_1(h_1 + h_3)[\varepsilon_2 - 1] - h_1[\varepsilon_2 - \varepsilon_1] - \varepsilon_2\varepsilon_1 d]^2}\right] \tag{4}$$

$$\pi_2 = \frac{\partial(-\Delta G)}{\partial h_3} = -\left[\frac{\varepsilon_0\varepsilon_1{}^2\varepsilon_2\psi^2[1 - \varepsilon_2]}{2[\varepsilon_1(h_1 + h_3)[\varepsilon_2 - 1] - h_1[\varepsilon_2 - \varepsilon_1] - \varepsilon_2\varepsilon_1 d]^2}\right] \tag{5}$$

Here, ε_0 is the permittivity of the vacuum.

D. Linear Theory. The LSA is carried out under the following two assumptions: (i) the kinematics of deformation of the films is treated using a small-deformation formulation, and (ii) the disjoining pressures are expanded in Taylor series about the base state and terms up to first order are retained.

$$\pi_1(h_{10} + \delta_1, h_{20} + \delta_2) = \pi_1(h_{10}, h_{20}) + [(\partial\pi_1/\partial h_1)|_{h_{10}, h_{20}}\delta_1 + (\partial\pi_1/\partial h_2)|_{h_{10}, h_{20}}\delta_2 + ...]$$

$$\pi_2(h_{10} + \delta_1, h_{20} + \delta_2) = \pi_2(h_{10}, h_{20}) + [(\partial\pi_2/\partial h_1)|_{h_{10}, h_{20}}\delta_1 + (\partial\pi_2/\partial h_2)|_{h_{10}, h_{20}}\delta_2 + ...] \tag{6}$$

where δ_1 and δ_2 are the infinitesimal perturbation at the elastic−elastic and elastic-air interface, respectively. In order to perform LSA, the governing differential equations are linearized using the normal linear modes, $\mathbf{u}_i = \tilde{\mathbf{u}}_i e^{wt+ikx}$, $P_i = \tilde{P}_i e^{wt+ikx}$, and $h_i = h_{i0} + \tilde{\delta}_i e^{wt+ikx}$ where the symbols ω and k represent the linear growth coefficient and the wavenumber of disturbance, respectively. Eliminating $\tilde{P}_i$ from the linearized governing equations (eq 1) results in a biharmonic equation for each of the two layers:

$$\frac{d^4\tilde{u}_i^z}{dz^4} - 2k^2\frac{d^2\tilde{u}_i^z}{dz^2} + k^4\tilde{u}_i^z = 0 \quad (7)$$

The general solution of eq 7 is

$$\tilde{u}_i^z = (B_{1i} + B_{2i}z)e^{kz} + (B_{3i} + B_{4i}z)e^{-kz} \quad (8)$$

where the coefficients B_{ji} ($j = 1-4$) are constants. Replacing the expressions for $\tilde{u}_i^{(z)}$, $\tilde{u}_i^{(x)}$ and $\tilde{P}_i$ in the linearized boundary conditions lead to a set of eight homogeneous linear algebraic equations involving eight unknown constants B_{ij} ($i = 1$ and 2, j = 1−4). Equating the determinant of the coefficient matrix of the set of linear equations to zero, the dispersion relation for the elastic bilayer is obtained [eq ix in the Appendix]. The details of the derivation are supplied in the Appendix. The general dispersion relation is then solved for the applied voltage $\psi = f(k)$. The critical condition for instability is obtained by determining the minimum voltage (ψ_c) from the dispersion relation. The wavenumber (k_c) corresponding to ψ_c gives the length scale ($\lambda_c = 2\pi/k_c$) of the instability. The derivation is done employing the commercial package Mathematica.

2. Viscous Bilayer. *A. Nonlinear Equation.* The coupled evolution equations for the liquid−liquid and liquid−air interfaces are derived under the assumptions that (i) the layers are thin enough that convective terms can be neglected and (ii) the long-wave approximation is valid because all interfaces deformations have small slope. Thus, starting with the Stokes equations, $\mu_i v_{i\,zz}^x = (p_i + \phi_i)_x$ and $\mu_i v_{i\,zz}^x = (p_i + \phi_i)_y$, the equations of continuity, $v_i^x + v_i^y + v_i^z = 0$, the kinematic boundary conditions for the individual layers $h_{it} + v_i^x|_{at\,h_i h_{ix}} + v_i^y|_{at\,h_i h_{iy}} = v_i^z|_{at\,h_i}$, and the velocity and stress boundary conditions at the two interfaces, we obtain the equations for the interfaces, $h_i = h_i(x,y,t)$. The boundary conditions employed for this derivation are as follows: $\mu_2 v_{2z}^x = 0, \mu_2 v_{2z}^y = 0$ at $z = h_2$ (zero shear at liquid−air interface); $v_2^x = v_1^x$, $v_2^y = v_1^y$, $v_2^z = v_1^z, \mu_2 v_{2z}^x = \mu_1 v_{1z}^x, \mu_2 v_{2z}^y = \mu_1 v_{1z}^y$, all at $z = h_1$ (continuity of velocity and shear stress at liquid−liquid interface); and $v_1^x = v_1^y = v_1^z = 0$ at $z = 0$ (no-slip and impermeability at the solid−liquid interface). Details of the derivation of the 2-D case are given elsewhere.[78] The resulting evolution equations are

$$\frac{\partial h_1}{\partial t} - \nabla\cdot\left[\left(\frac{(h_1)^3}{3\mu_1}\nabla P_1\right) + \left(\frac{h_1{}^2(h_2 - h_1)}{2\mu_1}\nabla P_2\right)\right] = 0 \quad (9)$$

$$\frac{\partial h_2}{\partial t} - \nabla\cdot\left[\left[\frac{(h_2 - h_1)^3}{3\mu_2} + \frac{(h_2 - h_1)h_1}{\mu_1}\left(h_2 - \frac{h_1}{2}\right)\right]\nabla P_2 + \left[\frac{h_1{}^2}{2\mu_1}\left(h_2 - \frac{h_1}{3}\right)\right]\nabla P_1\right] = 0 \quad (10)$$

Equations 9 and 10 describe the stability, dynamics, and morphology of the liquid−liquid ($i = 1$) and the liquid−air ($i = 2$) interfaces. The effective pressures at the liquid−liquid and liquid−air interfaces are derived from the normal stress balances at the respective interfaces as

$$P_1 = p_1 + \phi_1 = p_2 - \gamma_{21}\nabla^2 h_1 - \pi_1 \quad (11)$$

$$P_2 = p_2 + \phi_2 = p_0 - \gamma_2\nabla^2 h_2 - \pi_2 \quad (12)$$

Here P_0 is the ambient gas pressure, and π_1 and π_2 are the excess pressures resulting from the electric field. They are given by eqs 4 and 5, respectively. To capture the long-time dynamics for the viscous films and remove the contact-line singularities in the nonlinear analysis, we introduce short-range repulsion in the following manner:

$$\Delta G = \frac{\varepsilon_0\varepsilon_1\varepsilon_2\psi^2}{2}\left[\frac{1}{[(h_1 + h_3)\varepsilon_1[\varepsilon_2 - 1] - h_1[\varepsilon_2 - \varepsilon_1] - \varepsilon_2\varepsilon_1 d]}\right] + \frac{B_1}{(d - h_1 - h_3)^3} + \frac{B_2}{h_1{}^3} + \frac{B_3}{h_3{}^3} \quad (13)$$

Here we use a "softer" repulsive potential[12] for the ease of numerical computations. The expressions for B_1 and B_2 are obtained by imposing the minimum of the free energy [$\pi_1 = \partial(-\Delta G)/\partial h_1 = 0$] at $h_1 = l_0$ and $(d - h_2) = l_0$. The expressions for B_1 and B_3 are obtained by imposing the minimum of free energy [$\pi_2 = \partial(-\Delta G)/\partial h_3 = 0$] at $h_3 = l_0$ and $(d - h_2) = l_0$.

B. Linear Stability Analysis. Perturbing the interfaces by the linear normal modes, $h_i = h_{i0} + \delta_i e^{wt}\cos kx$, the dispersion relation is obtained by linearizing eqs 9 and 10:[78]

$$\omega = \frac{-(B + C) \pm \sqrt{(B - C)^2 + 4AD}}{2} \quad (14)$$

Here,

$$A = [(h_{10}^3/3\mu_1)(\gamma_2 k^4 - k^2\pi_{1h_2})] + [(1/2\mu_1)(h_{20} - h_{10})h_{10}^2(\gamma_2 k^4 - k^2\pi_{2h_2})]$$

$$B = [(h_{10}^3/3\mu_1)(\gamma_{21} k^4 - k^2\pi_{1h_1})] - [(1/2\mu_1)(h_{20} - h_{10})h_{10}^2(k^2\pi_{2h_1})]$$

$$C = [(1/2\mu_1)h_{10}^2(h_{20} - h_{10}/3)(\gamma_2 k^4 - k^2\pi_{1h_2})] + [(1/3\mu_2)(h_{20} - h_{10})^3 + (1/\mu_1)h_{10}(h_{20} - h_{10})(h_{20} - h_{10}/2)](\gamma_2 k^4 - k^2\pi_{2h_2})$$

$$D = [(1/2\mu_1)h_{10}^2(h_{20} - h_{10}/3)(\gamma_{21} k^4 - k^2\pi_{1h_1})] - [(1/3\mu_2)(h_{20} - h_{10})^3 + (1/\mu_1)h_{10}(h_{20} - h_{10})(h_{20} - h_{10}/2)](k^2\pi_{2h_1})$$

Here, δ_1 and δ_2 represent the infinitesimal amplitudes of the initial interface perturbations. The $\pi_{jh_i} = (\partial\pi_j/\partial h_i)$ are evaluated at mean thicknesses h_{10} and h_{20}, where j and i are indices representing films 1 or 2. The dominant wavelength ($\lambda_m = 2\pi/k_m$) corresponds to the fastest growth rate of disturbance (ω_m) and is obtained from the condition $\partial\omega/\partial k = 0$. The deformation mode induced by the electric field and the resulting relative amplitudes at the two

interface deformations correspond to the sign and the magnitude of the ratio of the linear amplitudes $\delta_r = \delta_2/\delta_1$, respectively. A detailed derivation of the expression for $\delta_r = -(\omega_m + B)/A = -D/(\omega_m + C)$ is given elsewhere.[78,81] In particular, $\delta_r < 0$ and $\delta_r > 0$ correspond to the *squeezing* and *bending* mode of deformation, respectively. Thereby, the upper interface deforms more (less) than the lower one when $|\delta_r| > 1$ ($|\delta_r| < 1$).

C. Solution of the Nonlinear Equations: Numerical Methods. The evolution eqs 9 and 10 are nondimensionalized for a compact representation of numerical results by introducing $X = K^{1/2}(x/h_{10})$; $Y = K^{1/2}(y/h_{10})$; $T = (\gamma_{21}K^2/3\mu_1 h_{10})t$; $H_1 = h_1/h_{10}$; $H_2 = h_2/h_{10}$; $D = d/h_{10}$; $M = \gamma_2/\gamma_{21}$; $R = \mu_1/\mu_2$; $\overline{P}_1 = P_1 h_{10}/K_1\gamma_{21}$; $\overline{P}_2 = P_2 h_{10}/K_1\gamma_{21}$; and $K = (\varepsilon_0\psi_b^2/2\gamma_{21}h_{10})$.

$$H_{1T} - \nabla\cdot[H_1^3\nabla\overline{P}_1] - \frac{3}{2}\nabla\cdot[H_1^2(H_2 - H_1)\nabla\overline{P}_2] = 0 \qquad (15)$$

$$H_{2T} - \nabla\cdot\left[\frac{3}{2}H_1^2\left(H_2 - \frac{H_1}{3}\right)\nabla\overline{P}_1\right] - \nabla\cdot\left[\left[R(H_2 - H_1)^3 + 3(H_2 - H_1)H_1\left(H_2 - \frac{H_1}{2}\right)\right]\nabla\overline{P}_2\right] = 0 \qquad (16)$$

Equations 15 and 16 are discretized using a central difference scheme with half node interpolation. The resulting set of coupled stiff ordinary differential equations in time is solved using Gear's algorithm with a volume preserving initial random perturbation and periodic boundary conditions in space. The grid independence of the solutions is ensured by varying the number of grid points.

It may be noted that all the simulations shown below use the nondimensional coordinates, X and Y, which are highly compressed compared to the nondimensional film thickness (~1). Thus, the slopes, $(\partial H/\partial X)$, are highly exaggerated in these figures, even though the dimensional slopes are small in conformity with the long-wave theory.

III. Results and Discussion

The application of a static electric field across the interface of two dielectric materials generates an additional stress because of the charge separation. The generated electrical stresses invoke a deformation of the interface as a measure of stress-relaxation. Deep in the nonlinear regime of evolution, the interface deforms more toward the material of lower dielectric constant. Thus, when a bilayer of dielectric liquids (Figure 1) is subjected to an electric field, the interface between the upper layer and air always deforms more toward the upper electrode because the dielectric constant of the upper film is large as compared to the one of air ($\varepsilon_2 > \varepsilon_g$). In contrast, the interface between the upper and lower layer can deform more either toward the upper electrode ($\varepsilon_1 > \varepsilon_2$) or toward the substrate ($\varepsilon_1 < \varepsilon_2$). The relative strength of the electric field and the hydrodynamic forces play an important role in the growth of the instability. For example, an increase of the strength of the elastic, viscous, or capillary force leads to a slower kinetics of destabilization, whereas an increase in the voltage (ψ) or a reduction of the separation distance between the electrodes (d) leads to a stronger destabilizing electric field and hence to a faster growth of the instability. In the following, we illustrate the key features of the instability for (i) elastic and (ii) viscous bilayers. The time and length scales of the instability are determined employing linear theory, whereas the morphological evolution of viscous bilayers is studied through a series of 2-D and 3-D nonlinear simulations.

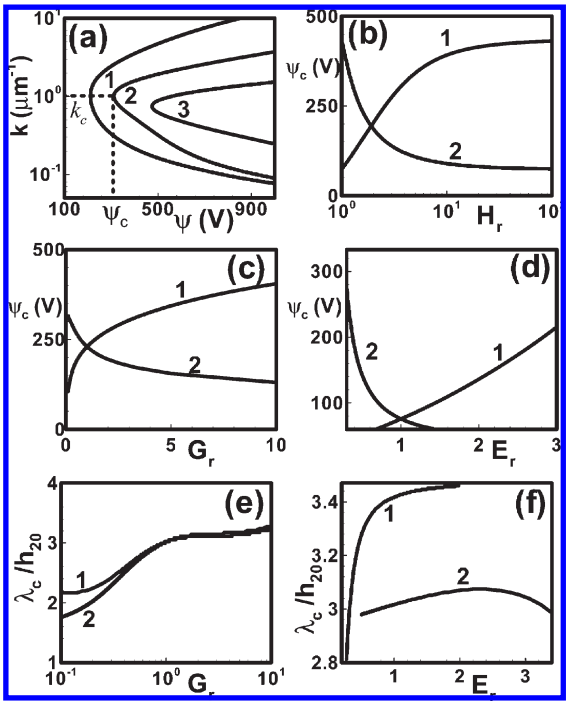

Figure 2. LSA results for elastic bilayers under the influence of an electrical field. Plot a shows the variation of k with ψ. Curves 1−3 represent $G_2 = 10^5$, 10^6, and 10^7 Pa at constant $G_1 = 10^5$ Pa. Plots b−d show the variations of ψ_c with H_r ($= h_{30}/h_{10}$), G_r ($= G_2/G_1$), and E_r ($= \varepsilon_2/\varepsilon_1$), respectively, and plots e−f show the variations of λ_c/h_{20} with G_r and E_r, respectively. In plot b, curves 1 and 2 correspond to $\varepsilon_1(= 5.5) > \varepsilon_2(= 2.0)$ and $\varepsilon_1(= 2.0) < \varepsilon_2(= 5.5)$, respectively, at constant $G_1 = G_2 = 10^5$ Pa and an air gap between the upper layer and the top electrode ($d - h_{20}$) of 100 nm. In plots c and e, curves 1 and 2 correspond to $G_1 = 10^6$ and $G_2 = 10^6$ Pa, respectively, when $\varepsilon_1 = \varepsilon_2 = 5.5$. In plots d and f, curves 1 and 2 correspond to $\varepsilon_1(= 5.5)$ and $\varepsilon_2(= 5.5)$ when G_1 and G_2 are kept constant at 10^5 Pa. The remaining parameters in a, b, and d are $h_{10} = 1\,\mu$m, $h_{20} = 2\,\mu$m, and $d = 2.1\,\mu$m. For all plots, $\varepsilon_0 = 8.85 \times 10^{-12}$ C^2/N m^2, $\gamma_2 = 0.03$ N/m, and $\gamma_{12} = 0.000015$ N/m.

1. Elastic Bilayers. *A. Linear Stability Analysis*. In this section, we employ LSA to explore the salient features of the electric-field-induced instabilities in thin elastic bilayers. The critical conditions to initiate the instabilities are identified and the variation of their wavelength with the ratio of the shear moduli and the dielectric permittivities is demonstrated.

Figure 2 shows the LSA results obtained for the elastic bilayer (as sketched in Figure 1) under the influence of an electric field. Curves 1−3 in Figure 2a represent borders of stability in the (k, ψ) plane obtained from dispersion relation. The *bifurcation point* (denoted by ψ_c and k_c in Figure 2a) corresponds to the *critical voltage* (ψ_c) required to initiate instability. Under this condition, the destabilizing forces exactly balance the stabilizing forces. An infinitesimal increase in the strength of the electric field from this value leads to the roughening of the interfaces with a lateral length scale of λ_c ($= 2\pi/k_c$). The critical voltage required to instigate the instability changes with the ratio of the thicknesses, shear moduli, and dielectric permittivities of the two layers. Figure 2b shows the variation of ψ_c with H_r ($= h_{30}/h_{10}$). Curve 1 represents the case $\varepsilon_1 > \varepsilon_2$, and curve 2 represents the case $\varepsilon_1 < \varepsilon_2$. The curves reveal that the critical voltage decreases with the increase of the thickness of the film that consists of the material of higher permittivity (the other thickness is fixed). This is due to an accompanying increase

in the total capacitance of the system, which eventually increases the strength of the destabilizing electric field. Figure 2c shows the variation of ψ_c with G_r (= G_2/G_1). It indicates that an increase in the shear modulus of the upper (curve 1, increasing G_r) or the lower layer (curve 2, decreasing G_r) stabilizes the bilayers, i.e., it increases the critical voltage. Curves 1 and 2 in Figure 2d show that ψ_c decreases when the capacitance of the bilayer is increased by increasing the dielectric permittivity of any of the films. Figure 2e and 2f depict the variations of normalized wavelength (λ_c/h_{20}) with G_r(= G_2/G_1) and E_r (= $\varepsilon_2/\varepsilon_1$), respectively. It shows that, compared to the simple law $\lambda_c \sim 3h$ for single elastic films, elastic bilayers show a considerable change in the wavelength when the ratio of the shear moduli and dielectric permittivities are changed. For example, Figure 2e shows that at $H_r = 1$ and $E_r = 1$, a soft upper film (10^6 Pa) on a relatively hard lower film (2×10^7 Pa) results in a smaller wavelength ($\lambda_c \sim 1.5h_{20}$) than a very hard (10^7 Pa) upper film resting on a softer lower film (10^6 Pa) that leads to $\lambda_c \sim 3.5h_{20}$. Note that, for identical shear moduli, the wavelength is $\lambda_c \sim 3h_{20}$ (Figure 2e), which corresponds to the correct single film limit (for $E_r = 1$). Figure 2f shows that changing E_r can also alter the length scale of the instabilities. For example, at $H_r = 1$ and $G_r = 1$, one finds $\lambda_c \sim 2.5h_{20}$ at low E_r. However, at high E_r, it can increase to $\lambda_c \sim 3.5h_{20}$ (curve 1). Thus, to reduce the critical voltage required to initiate the instability or to reduce the corresponding wavelength of patterns, one may increase the thickness of the material with the larger dielectric constant, or compose the bilayer of materials with larger dielectric permittivities and/or lower shear moduli.

2. Viscous Bilayers. In this section, we explore the key features of the electric-field-induced instabilities in thin viscous bilayers. Unlike elastic bilayers, the viscous bilayers readily deform under the influence of a destabilizing electric field. In this section, first, we discuss the LSA results, which show the variations in the length and time scales of the instabilities with the thicknesses and the dielectric permittivities of the films. Thereafter, we study the nonlinear evolution of the unstable interfaces. The results obtained from the simulations are compared to the available experimental results.

A. Linear Stability Analysis. Figure 3 summarizes the LSA results when the film thicknesses are varied. Figure 3a,b shows the dependence of the linear growth coefficient (ω) on wavenumber (k). Figure 3c,e shows the variations of the maximal growth coefficient (ω_m) with the thickness ratio H_r(= h_{30}/h_{10}). Figure 3d,f shows the variations of the wavelength (λ_m) with H_r. In all Figure 3c−f, the solid and the dashed lines correspond to $\varepsilon_1 > \varepsilon_2$ and $\varepsilon_1 < \varepsilon_2$, respectively.

In Figure 3a−d, the composite film thickness (h_{20}) is kept constant, and the ratio h_{30}/h_{10} is varied. For $\varepsilon_1 > \varepsilon_2$, Figure 3c,d shows (solid lines) that ω_m increases and λ_m decreases for a decreasing thickness ratio of upper and lower layer. An increase in h_{10} (decreasing H_r) enhances the capacitance and hence the electrical stresses at the interfaces, thereby reducing the time and length scales of the instability. The dashed line in Figure 3c,d shows that, when the upper layer has higher dielectric constant ($\varepsilon_1 < \varepsilon_2$), an increase in h_{10} (decreasing H_r) reduces the capacitance of the bilayer, which results in the progressive reduction of ω_m and λ_m. Figure 3e,f looks at another scenario, in particular, when the gap between the electrodes (d) and one of the film thicknesses is varied (h_{30} or h_{10}), whereas the other one is kept constant. Curve 1 in Figure 3e,f indicates that, keeping h_{10} constant for $\varepsilon_1 > \varepsilon_2$, an increase in h_{30} (increasing H_r) leads to a reduction of the air gap between the upper layer and the top electrode. This causes an increase in ω_m and reduces λ_m. For $\varepsilon_1 > \varepsilon_2$, curve 2 shows a progressive increase in ω_m and decrease of λ_m

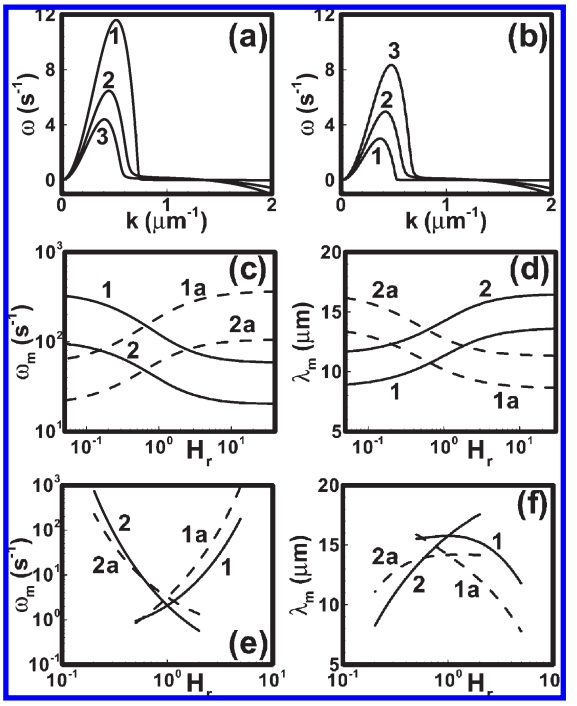

Figure 3. LSA results for the viscous bilayers under the influence of an electrical field. Plots a and b show the variation of ω with k for ε_1(= 2.0) < ε_2 (= 3.0) and ε_1 (= 3.0) > ε_2(= 2.0), respectively, at constant h_{20} = 250 nm. Curves 1−3 in plot a correspond to h_{10} = 25 nm, 150 nm, and 200 nm, and in plot b they correspond to h_{10} = 25 nm, 125 nm, and 200 nm, respectively. Plots c and d show the variations of ω_m and λ_m, respectively, with H_r (= h_{30}/h_{10}) at constant h_{20}. Curves 1, 1a and 2, 2a correspond to h_{20} = 500 nm, and 400 nm, respectively. Plots e and f show the variations of ω_m and λ_m, respectively, with H_r. In plots e and f, curves 1 and 1a correspond to constant h_{10} = 100 nm, and curves 2 and 2a correspond to h_{30} = 100 nm. In plots c, d, e, and f, the solid lines correspond to ε_1(= 3.0) > ε_2(= 2.0), and the dashed lines correspond to ε_1(= 2.0) < ε_2(= 3.0). The other necessary parameters used for all these plots are shown in SET I of Table 1.

with increasing h_{10} (decreasing H_r) at constant h_{30}. In comparison, curve 1a shows that bilayers with $\varepsilon_1 < \varepsilon_2$ can be more unstable (larger ω_m) because an increase in h_{30} leads to a larger total capacitance of the bilayer. Similarly, curve 2a shows that bilayers with $\varepsilon_1 < \varepsilon_2$ are more stable (smaller ω_m) when h_{10} is relatively large (small H_r).

Figure 4 summarizes the LSA results when the dielectric constants are varied for constant film thicknesses. Figure 4a,b shows selected ω versus k plots at constant $\varepsilon_1 > \varepsilon_2$ and constant $\varepsilon_2 > \varepsilon_1$, respectively. Figure 4c,d shows the variation of ω_m, Figure 4e,f shows the variation of λ_m, and Figure 4g,h show the variation of the relative deformations of the interfaces δ_r with $E_r = \varepsilon_2/\varepsilon_1$. The ω versus k plots in Figure 4a,b are bimodal in nature, i.e., they have two maxima. The higher one represents the dominant mode. Figure 4a,b shows that, in both cases, $\varepsilon_1 > \varepsilon_2$ (Figure 4a) and $\varepsilon_2 > \varepsilon_1$ (Figure 4b), the large (small) wavenumber mode dominates for larger (smaller) permittivity contrast. The shift of the dominant mode of instability from larger to smaller wavenumber mode with E_r results in the discontinuities visible in Figure 4c−f. Figure 4g indicates that, when $\varepsilon_2 < \varepsilon_1$, the interfaces always deform in *bending* mode ($\delta_r > 0$), and the deformation at the liquid−liquid interface is much larger ($\delta_r \ll 1$) when $\varepsilon_2 \ll \varepsilon_1$ (low E_r). The wavelength of instability in this case is smaller (low E_r in Figure 4e) because of the smaller interfacial tension at the liquid−liquid interface. However, when ε_2 is progressively increased at constant ε_1, the stronger deflection shifts to the

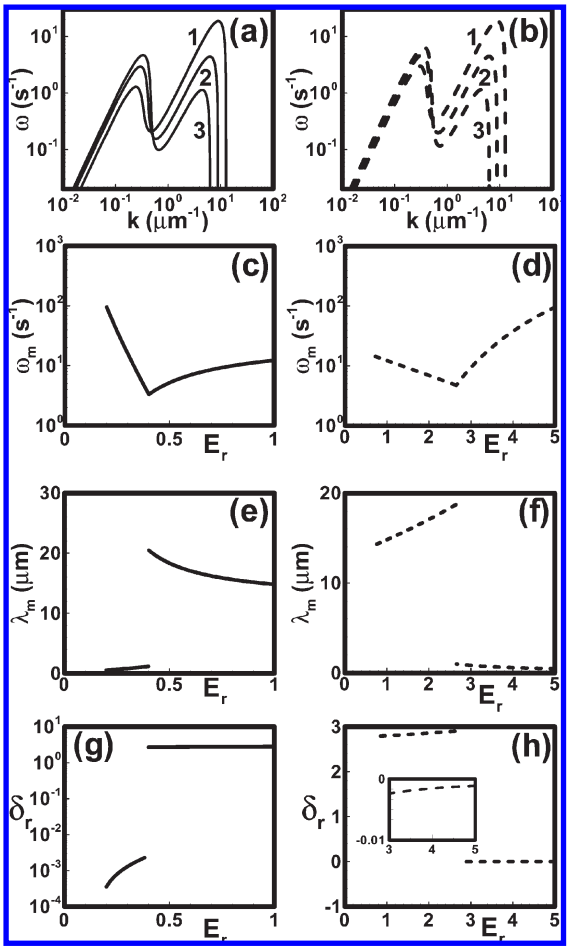

Figure 4. LSA results for the viscous bilayers under the influence of an electrical field. Plots a and b show the variation of ω with k. Curves 1−3 in plot a correspond to $\varepsilon_2 = 1.6$, 2.1, and 2.6, respectively, at constant $\varepsilon_1 = 5.5$. In plot b, they correspond to $\varepsilon_1 = 1.6$, 2.1, and 2.6, respectively, at constant $\varepsilon_2 = 5.5$. Plots c and d show the variation of ω_m with E_r ($= \varepsilon_2/\varepsilon_1$), plots e and f show the variation of λ_m with E_r, and plots g and h show the variation of δ_r with E_r. In all the plots, the solid lines correspond to $\varepsilon_1 = 5.5$, and the dashed lines correspond to $\varepsilon_2 = 5.5$. The other parameters are shown in SET II of Table 1.

liquid−air interface ($\delta_r > 1$), and the instability grows with a larger wavelength because of the larger interfacial tension at the liquid−air interface (high E_r in Figure 4e). In comparison, Figure 4h indicates that, when $\varepsilon_2 > \varepsilon_1$, the interfaces deform in the *squeezing* mode ($\delta_r < 0$ as shown in the inset). The deformation at the liquid−liquid interface is much larger ($\delta_r \ll 1$) when $\varepsilon_2 \gg \varepsilon_1$ (high E_r). Again, the dominant wavelength of instability in this case is smaller (high E_r in Figure 4f) because of the smaller interfacial tension at the liquid−liquid interface. At a larger value of ε_1, the stronger deflection shifts to the liquid−air interface ($\delta_r > 1$), and instability grows with a larger wavelength (low E_r in Figure 4f).

B. Morphological Evolution of Interfaces. The nonlinear time evolution described by eqs 15 and 16 is simulated to verify and extend the results obtained from the linear analysis. In particular, we focus on the growth of the two qualitatively different linear modes (*squeezing* and *bending*) of instability at the early stages of evolution and the subsequent long-time morphologies. All the simulations presented here show different important features of the electric-field-induced structural evolution prior to the actual rupture of the films. It should also be noted that the long-wave bilayer equations cease to be valid when the top film ruptures and the fluid−fluid and fluid−gas interfaces coalesce. The subsequent experimentally possible "leakage" of the bottom fluid to cover the top surface implies the formation of a new interface, and a multivalued function for the thickness of the bottom layer arises. This situation goes well beyond the capacities of the long-wave model of two layers of immiscible fluids employed here and elsewhere.[74−88] In particular, a true encapsulation of the top fluid by the bottom fluid cannot be studied. However, the stages of the evolution close to rupture captured here already point to imminent layer inversion and encapsulation. The typical parameter values used for the nonlinear analyses correspond to those of previous experimental work[39,45] and are listed in Table 1.

Table 1. Typical Values of Bilayer Parameters

variables	SET I	SET II
ε_0 (C^2/N m^2)	8.85×10^{-12}	8.85×10^{-12}
ψ (V)	50	140
γ_{21} (N/m)	0.0007	0.000015
γ_2 (N/m)	0.03	0.03
μ_2 (Pa s)	1	2.3×10^5
μ_1 (Pa s)	1	24
d (nm)	1000	3000
h_{10} (nm)	150	500
h_{30} (nm)	100	500

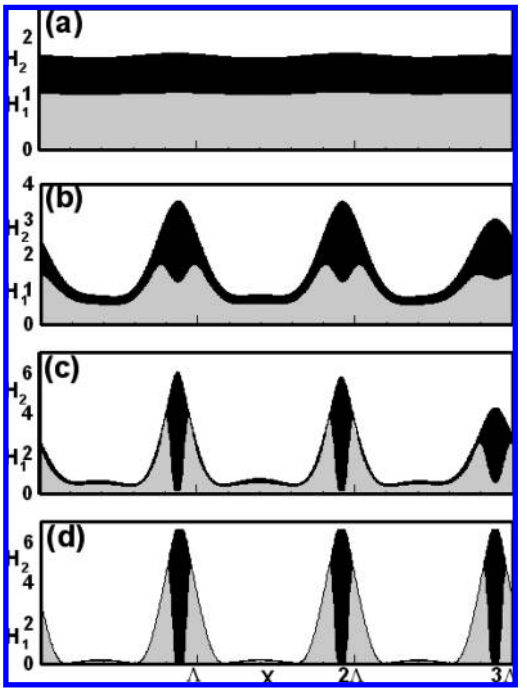

Figure 5. 2-D spatiotemporal evolution of instability of a SET I bilayer for an $L = 3\,\Lambda$ domain when $\varepsilon_1 = 2.0$ and $\varepsilon_2 = 3.0$. The initial amplitudes are $\delta_1 = \delta_2 = 0.05$. Snapshots are given at times (a) $T = 7.9 \times 10^6$, (b) $T = 1.8 \times 10^7$, (c) $T = 2.1 \times 10^7$, and (d) $T = 7.7 \times 10^8$.

Figures 5 and 6 show 2-D and 3-D nonlinear simulations, respectively, of a SET I bilayer with $\varepsilon_2 > \varepsilon_1$. Here, Λ is the dimensionless dominant wavelength corresponding to the maximum growth rate of the instability obtained from the linear LSA. The instability starts as a *bending* mode of the interfaces (Figure 5a and images 6I). Thereafter, the upper layer forms periodic columnar structures because in the nonlinear regime of evolution a higher dielectric constant of the upper layer ($\varepsilon_2 > \varepsilon_g$) leads to a larger upward than downward deformation of the liquid−air interface (Figure 5b and image 6II). It is also interest-

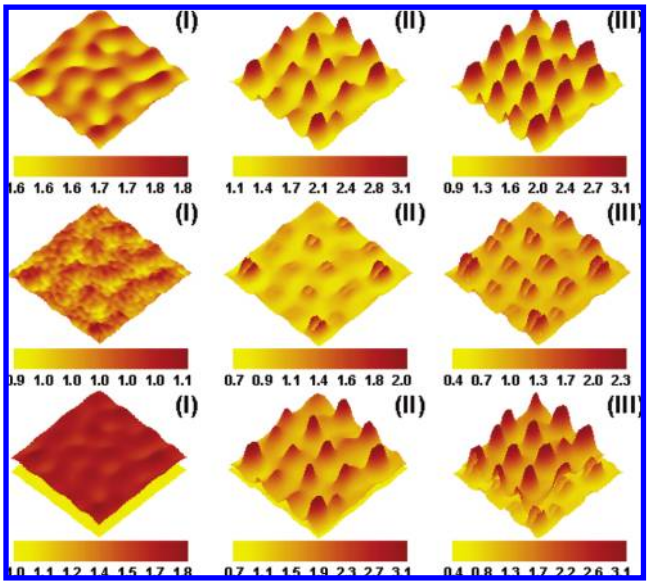

Figure 6. 3-D spatiotemporal evolution of instability of a SET I bilayer for an $L = 4\ \Lambda$ domain when $\varepsilon_1 = 2.0$ and $\varepsilon_2 = 3.0$. The remaining parameters are $\delta_1 = \delta_2 = 0.05$ and $d = 500$ nm. The first, second, and third row present the liquid−air interface, liquid−liquid interface, and the composite images, respectively. The images correspond to times (I) $T = 3.34 \times 10^4$, (II) $T = 5.34 \times 10^4$, and (III) $T = 5.75 \times 10^4$. Lighter shades of yellow represent the lower thickness regions.

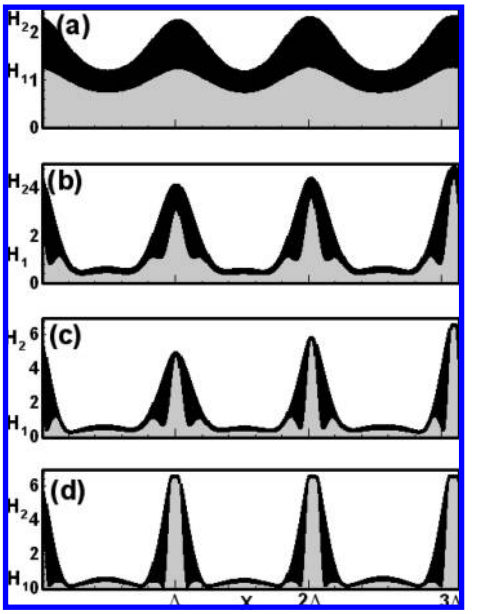

Figure 7. 2-D spatiotemporal evolution of instability of a SET I bilayer for an $L = 3\ \Lambda$ domain when $\varepsilon_1 = 3.0$ and $\varepsilon_2 = 2.0$. The initial amplitudes are $\delta_1 = \delta_2 = 0.05$. Snapshots are given at times (a) $T = 1.37 \times 10^7$, (b) $T = 1.95 \times 10^7$, (c) $T = 2.08 \times 10^7$, and (d) $T = 3.8 \times 10^7$.

ing to note that the linear bending mode no longer prevails in the nonlinear regime. The larger dielectric permittivity of the upper layer ($\varepsilon_2 > \varepsilon_1$) causes a zone of downward depression of the liquid−liquid interface under each column formed by the upper layer (Figure 5b and image 6II). Subsequently, the columns of upper liquid almost reach down to the substrate, while the lower layer liquid starts to encapsulate them (Figure 5c). At the late stages of the evolution, the upper layer touches the top electrode and starts to spread on it, while the lower layer liquid forms beaker-like structures under the upper layer columns (image 6III). The sides of the beakers grow further toward the top electrode to encapsulate the columns (Figure 5d and image 6III). Note that the simulation shown in Figure 5 has parameters similar to the experimental ones of ref 39. The final morphologies shown in the Figure 5d and image 6III are very similar to the experimental results shown in Figures 1 and 2 of ref 39.

Figure 7 (Figure 8) shows a 2-D (3-D) nonlinear simulation of a bilayer similar to the one in Figure 5 (Figure 6), however, with the permittivity ratio reversed ($\varepsilon_2 < \varepsilon_1$). The choice of the dielectric constants ($\varepsilon_1 > \varepsilon_2 > \varepsilon_g$) now ensures that both interfaces deform more toward the top electrode in the nonlinear regime. The instability starts as a *bending* mode of the interfaces with a larger deformation at the liquid−air interface (Figure 7a and image 8I). As the evolution progresses, the liquid−air interface develops into columnar structures (Figure 7b and image 8II). At the late evolution stages, the lower layer also grows stronger toward the top electrode and, consequently, forms columnar structures (Figure 7c and image 8III). The final morphology shows an array of concentric columnar structures with a lower layer core and an outer-shell composed of the upper layer liquid. The final morphologies shown in Figures 5−8 reveal that interchanging the dielectric permittivities of the films can change the composition of the columnar structures from an upper layer encapsulated by a lower layer to lower layer encapsulated by an upper layer. As also seen in the case of a single layer destabilized by an electric field,[35,36,46−48,57] the structures show a hexagonal order, which

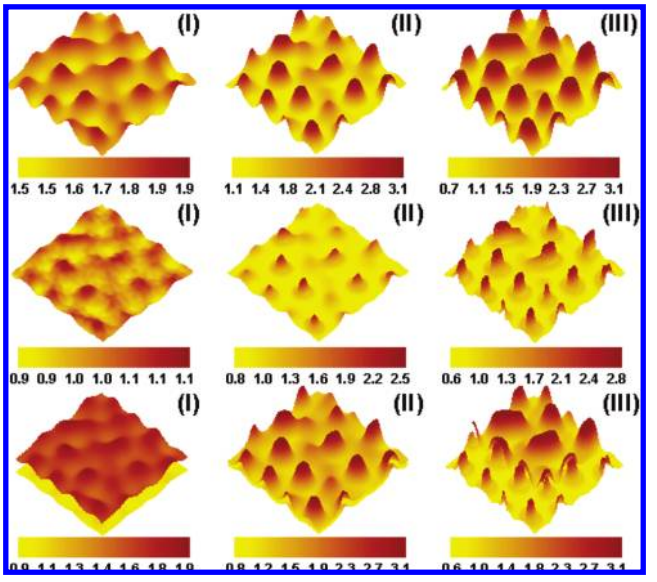

Figure 8. 3-D spatiotemporal evolution of instability of a SET I bilayer for an $L = 4\ \Lambda$ domain when $\varepsilon_1 = 3.0$ and $\varepsilon_2 = 2.0$. The remaining parameters are $\delta_1 = \delta_2 = 0.05$ and $d = 500$ nm. The first, second, and third row give the liquid−air interface, liquid−liquid interface, and the composite images, respectively. The images correspond to times (I) $T = 1.37 \times 10^7$, (II) $T = 1.95 \times 10^7$, and (III) $T = 3.8 \times 10^7$. Lighter shades of yellow represent the lower thickness regions.

may be less (Figure 8) or more (Figure 6) prominent depending on the conditions. The structure generated by a fast penetration of the upper layer in the lower fluid displays a higher degree of order in Figure 6, whereas a slower evolution of the core−shell structure in Figure 8 has more opportunity for ripening, leading to less order.

Figure 9 shows a collage of 2-D and 3-D nonlinear simulations of another interesting SET I bilayer. In contrast to the simulations discussed above, the choice of dielectric constants of the materials

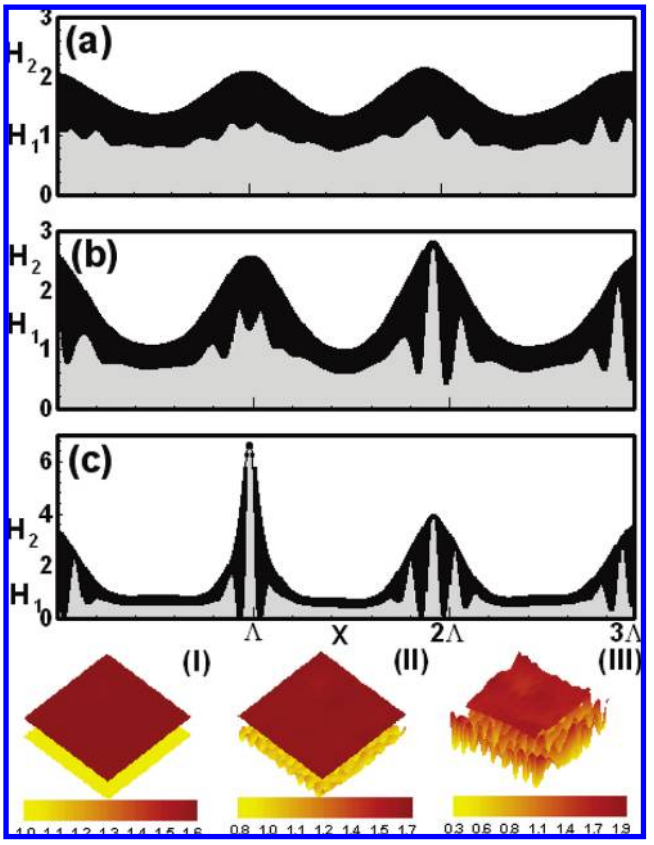

Figure 9. 2-D spatiotemporal evolution of instability of a SET I bilayer for an $L = 3\ \Lambda$ when $\varepsilon_1 = 5.0$ and $\varepsilon_2 = 1.5$. The initial amplitudes are $\delta_1 = \delta_2 = 0.05$. Snapshots are given at times (a) $T = 1.35 \times 10^7$, (b) $T = 1.64 \times 10^7$, and (c) $T = 1.90 \times 10^7$. Images I−III show 3-D spatiotemporal evolution of the same bilayer but with $d = 500$ nm. The images correspond to times (I) $T = 3.39 \times 10^3$, (II) $T = 2.66 \times 10^4$, and (III) $T = 4.58 \times 10^4$. Lighter shades represent the lower thickness regions in the 3-D simulations.

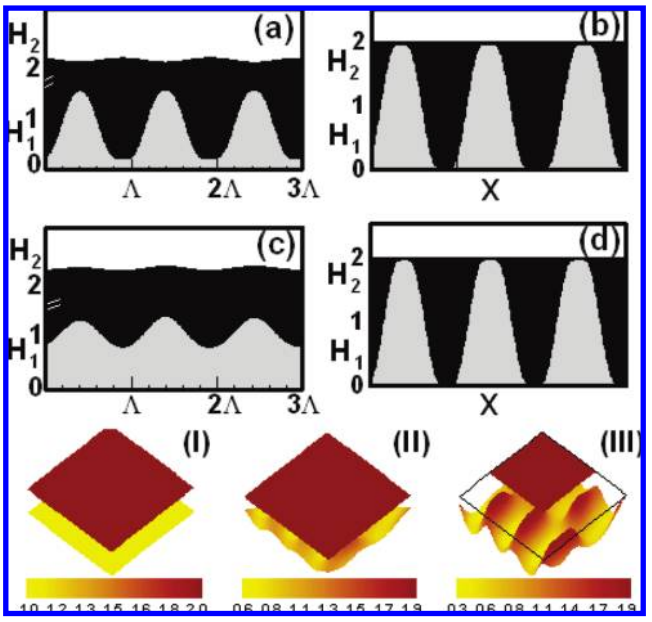

Figure 10. 2-D spatiotemporal evolution of instability of a SET II bilayer for an $L = 3\ \Lambda$ domain. Images a and b show the evolution when $\varepsilon_1 = 2.0$ and $\varepsilon_2 = 5.5$, whereas c and d correspond to $\varepsilon_1 = 5.5$ and $\varepsilon_2 = 2.0$. The initial amplitudes are$\delta_1 = \delta_2 = 0.05$. Snapshots are given at times (a) $T = 4.4 \times 10^8$, (b) $T = 2.7 \times 10^{10}$, (c) $T = 6.2 \times 10^7$and (d) $T = 6 \times 10^{10}$. Images I−III show 3-D spatiotemporal evolution of instability of a SET II bilayer system for an $L = 3\ \Lambda$ domain when $\varepsilon_1 = 5.5$ and $\varepsilon_2 = 2.0$. The images correspond to times (I) $T = 5.9 \times 10^4$, (II) $T = 1.3 \times 10^8$, and (III) $T = 1.6 \times 10^8$. Lighter shades represent the lower thickness regions in the 3-D simulations.

for this simulation ensures that ω versus k plots are bimodal in the LSA. In consequence, one observes that the two interfaces evolve with different wavelengths. The plots show that the liquid−liquid interface rapidly evolves the mode with the shorter wavelength. The smaller time and length scales result from the weaker stabilizing effect of its lower interfacial tension (Figure 9a and image 9I). In contrast, the larger interfacial tension at the liquid−air interface results in the evolution of a larger wavelength. As evolution progresses, the out-of-phase interfacial structures grow further (Figure 9b and image 9II). The faster growth of the lower layer structures late in the nonlinear regime of evolution can also be attributed to its weaker interfacial tension. The final morphology corresponds to an array of columnar structures of the lower layer embedded inside the modulated upper layer (Figure 9c and image 9III).

It is interesting that the interfacial morphologies can also be altered profoundly by changing the film viscosities, which are kinetic, rather than thermodynamic, parameters. One recent experimental study[45] has shown that a bilayer consisting of a high viscosity upper layer on a low viscosity lower layer can undergo a phase inversion of layers when subjected to an electric field. The parameters of the experimental study are listed as SET II in Table 1. Figure 10 shows 2-D and 3-D nonlinear simulations of a SET II bilayer. Figure 10a,b shows the case of a lower layer that has a very low dielectric permittivity as compared to the upper layer ($\varepsilon_2 > \varepsilon_1$). Figure 10a shows that the interfaces rapidly develop an asymmetric *squeezing* mode. Thereby the deformation is almost exclusively located at the liquid−liquid interface because of its smaller interfacial tension. This feature is in agreement with the LSA results of Figure 4. Then the deformation of the liquid−liquid interface increases further (Figure 10b) until it becomes clear that the evolution corresponds to the early stages of layer inversion. However, here the model breaks down when the lower liquid breaks through the liquid−air interface. Figure 10c,d shows that, when the lower layer has a very high dielectric permittivity as compared to the upper layer ($\varepsilon_2 < \varepsilon_1$), the instability starts as a *bending* mode. However, again the strong stresses because of the difference in the dielectric permittivities of the films and a smaller restoring surface tension lead to a larger deformation at the liquid−liquid interface (as predicted by LSA). The final morphology shows an array of columnar structures of the lower layer embedded in the upper layer. The 3-D evolution shown in images 10I−III demonstrate the early stages of layer inversion obtained by the experiments in ref 45, before the lower liquid interface breaks through the liquid−air interface.

Unlike the previous case shown above, reduction in the upper layer viscosity can also profoundly influence the final morphology. For example, Figure 11 shows a collage of 2-D and 3-D nonlinear simulations of a bilayer similar to that discussed in Figures 5 and 6, however, with a reduced upper layer viscosity. Reduction in the viscous resistance of the upper layer causes a faster destabilization of the upper film, which produces an array of columnar structures before the lower layer starts evolving (Figure 11a,b and image 11III). The morphological evolution shown in Figure 11 is similar to that found in the experiments of ref 41. Thus, the viscosity ratio in a bilayer has a profound influence not only on the dynamics, but also on the pathway of evolution and the resulting morphologies. This is in complete contrast to the evolution of a single thin film where the viscosity

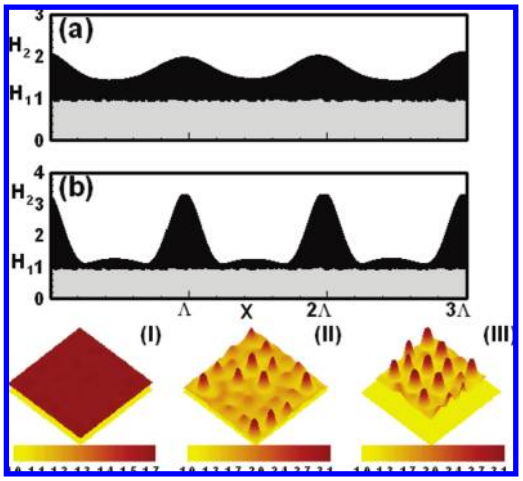

Figure 11. 2-D spatiotemporal evolution of instability of a SET I bilayer for an $L = 3\ \Lambda$ domain when $\varepsilon_1 = 2.0$ and $\varepsilon_2 = 3.0$. The initial amplitudes are $\delta_1 = \delta_2 = 0.05$. In plots a and b, $\mu_1 = 10^5$ kg/m s, $\mu_2 = 0.1$ kg/m s, and $d = 500$ nm. Times are (a) $T = 0.7$ and (b) $T = 1.24$. Images I−III show 3-D spatiotemporal evolution of the same bilayer with $d = 500$ nm for a domain size of $L = 5\ \Lambda$. The images correspond to times (I) $T = 0.17$, (II) $T = 0.67$, and (III) $T = 0.76$. Lighter shades represent the lower thickness regions in the 3-D simulations.

merely modifies the time scale of pattern evolution, but not the emerging morphology.

IV. Conclusions

We have presented a detailed linear analysis of interfacial instabilities of elastic and viscous bilayers due to an applied electric field. This has been followed by a long wave nonlinear analysis of the unstable evolution of viscous bilayers. The main features of the instabilities that have been obtained are as follows:

(i) The elastic bilayers provide a larger flexibility toward attaining patterns of diverse wavelength as compared to single-film systems because, apart from film thickness, the shear moduli and the dielectric permittivities of the films also play a crucial role in altering the length scale of the instability. In addition, our study has demonstrated that the destabilizing forces in the bilayers can be strengthened either by increasing the thickness of the material that has the larger dielectric constant or by composing the bilayer of materials that have larger dielectric permittivities and/or lower shear moduli. This can effectively reduce the critical voltage required to initiate the instability and the corresponding wavelength of patterns.

(ii) For viscous bilayers, the linear analysis has shown that a shorter unstable wavelength can be achieved by increasing the strength of the destabilizing forces. This can be done by increasing the thickness of the layer of the liquid with larger permittivity and by composing the bilayer employing liquids of larger dielectric permittivity.

(iii) The linear analysis together with nonlinear simulations have shown that the interfaces can evolve in *squeezing* mode when the ratio of the dielectric constants of the upper and the lower liquid layer ($E_r = \varepsilon_2/\varepsilon_1$) is high and the interfacial tension at the liquid−liquid interface is low. A larger difference in the dielectric permittivities ($\varepsilon_2 \gg \varepsilon_1$ or $\varepsilon_2 \ll \varepsilon_1$) of the films can also lead to out-of-phase deformations with two different wavelengths at the two interfaces. Otherwise, the bilayers evolve in the *bending* mode.

(iv) Nonlinear simulations have been used to investigate the details of the morphological evolution found in several experimental studies.[39,41,45] A number of interesting interfacial morphologies have been obtained under different conditions: (a) upper layer columns embedded in lower layer beakers (Figures 5 and 6), [39] (b) lower layer columns sheathed by the upper layer liquid resulting in concentric core−shell columns (Figures 7 and 8), (c) droplets of the upper liquid on a largely undisturbed lower layer (Figure 11),[41] and (d) structures of two different structure lengths at the two interfaces of a bilayers (Figure 9).

In summary, the theory presented in this work addresses many interesting scenarios of electric-field-induced instabilities in thin bilayers that are relevant for applications such as self-organized patterning, and micro- and nanofluidics. Previous simulations of a single liquid−air surface[48,54,57] or a single liquid−liquid[56] interface subjected to an electric field have resulted in a considerable understanding of experimental patterns. The results shown in this study have provided some very useful insights into the formation of complex structures in thin polymer bilayers as observed in experiments.[39,41,45] The main restriction of a long-wave bilayer theory is that it can not, in principle, be used for a study of layer inversion. The evolving free surface of a decomposing or decomposed mixture employing diffuse interface theory[93,94] can indeed model phase inversion of layers and is left as a future scope of research work.

Acknowledgment. D.B. acknowledges useful discussions with Ning Wu, V. Shankar, and G. Tomar. A.S. acknowledges the support of the DST through its grants to the Unit on Nanosciences at IIT Kanpur, a J. C. Bose Fellowship, and an IRHPA grant. U. T. acknowledges support by the European Union via the FP7 Marie Curie scheme [PITN-GA-2008-214919 (MULTIFLOW)].

Appendix

Linear Stability Analysis. The governing equations are linearized employing the normal linear modes $\mathbf{u}_i = \tilde{\mathbf{u}}_i e^{wt+\mathbf{i}kx}$, $P_i = \tilde{P}_i e^{wt+\mathbf{i}kx}$, and $h_i = h_{i0} + \tilde{\delta}_i e^{wt+\mathbf{i}kx}$:

$$-\mathbf{i}k\tilde{P}_i + G_i\left(-k^2\tilde{u}_i^x + \frac{\partial^2\tilde{u}_i^x}{\partial z^2}\right) = 0 \qquad \text{(i)}$$

$$-\frac{\partial\tilde{P}_i}{\partial z} + G_i\left(-k^2\tilde{u}_i^z + \frac{\partial^2\tilde{u}_i^z}{\partial z^2}\right) = 0 \qquad \text{(ii)}$$

$$\mathbf{i}k\tilde{u}_i^x + \frac{\partial\tilde{u}_i^z}{\partial z} = 0 \qquad \text{(iii)}$$

Eliminating $\tilde{P}_i$ from the linearized governing equations (eqs i−iii) results in a biharmonic equation for each of the two layers:

$$\frac{d^4\tilde{u}_i^z}{dz^4} - 2k^2\frac{d^2\tilde{u}_i^z}{dz^2} + k^4\tilde{u}_i^z = 0 \qquad \text{(iv)}$$

(91) Israelachvili, J. N. *Intermolecular and Surface Forces*; Academic Press: London, 1992.
(92) van Oss, C. J.; Chaudhury, M. K.; Good, R. J. *Chem. Rev.* **1988**, *88*, 927.
(93) Thiele, U.; Madruga, S.; Frastia, L. *Phys. Fluids* **2007**, *19*, 122106.
(94) Madruga, S.; Thiele, U. *Phys. Fluids*, in press.

The general solution of eq iv is

$$\tilde{u}_i^z = (B_{1i} + B_{2i}z)e^{kz} + (B_{3i} + B_{4i}z)e^{-kz} \quad \text{(v)}$$

Here the coefficients B_{ji} ($j = 1-4$) are constants. The expressions for the linearized boundary conditions are

$$\text{at } z = 0,\ \tilde{u}_1^x = \tilde{u}_1^z = 0 \quad \text{(vi)}$$

$$\text{at } z = h_1,\ \tilde{u}_1^x = \tilde{u}_2^x,\ \tilde{u}_1^z = \tilde{u}_2^z,\ G_1\left(\frac{\partial \tilde{u}_1^x}{\partial z} + \mathbf{i}k\tilde{u}_1^z\right) = G_2\left(\frac{\partial \tilde{u}_2^x}{\partial z} + \mathbf{i}k\tilde{u}_2^z\right),\ \tilde{\varepsilon}_1 = \tilde{u}_1^z|_{h_{10}},\ \text{and}$$

$$\tilde{P}_1 - \tilde{P}_2 - 2G_1\frac{\partial \tilde{u}_1^z}{\partial z} + 2G_2\frac{\partial \tilde{u}_2^z}{\partial z} + \left|\left(-k^2\gamma_{21} + \frac{\partial \pi_1}{\partial h_1} - \frac{\partial \pi_2}{\partial h_1}\right)\tilde{u}_1^z\right|_{h_{10}, h_{20}} + \left|\left(\frac{\partial \pi_1}{\partial h_2} - \frac{\partial \pi_2}{\partial h_2}\right)\tilde{u}_2^z\right|_{h_{10}, h_{20}} = 0 \quad \text{(vii)}$$

$$\text{at } z = h_2,\ G_2\left(\frac{\partial \tilde{u}_2^x}{\partial z} + \mathbf{i}k\tilde{u}_2^z\right) = 0,\ \tilde{P}_2 - 2G_2\frac{\partial \tilde{u}_2^z}{\partial z} + \left|\left(-k^2\gamma_2 + \frac{\partial \pi_2}{\partial h_2}\right)\tilde{u}_2^z\right|_{h_{10}, h_{20}} + \left(\frac{\partial \pi_2}{\partial h_1}\right)\tilde{u}_1^z\Big|_{h_{10}, h_{20}} = 0,\ \text{and}\ \tilde{\varepsilon}_2 = \tilde{u}_2^z\Big|_{h_{20}} \quad \text{(viii)}$$

Replacing the expressions for $\tilde{u}_i^z$, $\tilde{u}_i^x$, and $\tilde{P}_i$ in the linearized boundary conditions leads to a set of eight homogeneous linear algebraic equations involving eight unknown constants B_{ij} ($i = 1$ and 2, $j = 1-4$). Equating the determinant of the coefficient matrix of the set of linear equations to zero leads to the dispersion relation for the elastic bilayers:

$$\begin{vmatrix}
1 & -1 & \frac{1}{k} & \frac{1}{k} & 0 & 0 & 0 & 0 \\
1 & 1 & 0 & 0 & 0 & 0 & 0 & 0 \\
J_1 & -J_2 & \frac{J_1J_5}{k} & -\frac{J_2J_6}{k} & -J_1 & J_2 & -\frac{J_1J_5}{k} & \frac{J_2J_6}{k} \\
J_1 & J_2 & h_1J_1 & h_1J_2 & -J_1 & -J_2 & -h_1J_1 & -h_1J_2 \\
2kG_1J_1 & 2kG_1J_2 & 2G_1J_1J_5 & 2G_1J_2J_6 & -2kG_2J_1 & -2kG_2J_2 & -2G_2J_1J_5 & -2G_2J_2J_6 \\
0 & 0 & 0 & 0 & 2kG_2J_3 & 2kG_2J_4 & 2G_2J_{11}J_3 & 2G_2J_{12}J_4 \\
-J_1J_{10} & J_2J_7 & -h_1J_1J_{10} & h_1J_2J_7 & J_{13} & J_{14} & J_{15} & J_{16} \\
J_1\phi_2 & J_2\phi_2 & h_1J_1\phi_2 & h_1J_2\phi_2 & J_3J_8 & J_4J_9 & h_2J_3J_8 & h_2J_4J_9
\end{vmatrix} = 0 \quad \text{(ix)}$$

where $J_1 = e^{kh}{}_1$; $J_2 = e^{-kh}{}_1$; $J_3 = e^{kh}{}_2$; $J_4 = e^{-kh}{}_2$; $J_5 = (1 + kh_1)$; $J_6 = (-1 + kh_1)$; $J_7 = (2kG_1 - k^2\gamma_{12} + \phi_1)$; $J_8 = (-2kG_2 - k^2\gamma_2 + \phi_4)$; $J_9 = (2kG_2 - k^2\gamma_2 + \phi_4)$; $J_{10} = (2kG_1 + k^2\gamma_{12} - \phi_1)$; $J_{11} = (1 + kh_2)$; $J_{12} = (-1 + kh_2)$; $J_{13} = (2kG_2J_1 + J_3\phi_2)$; $J_{14} = (-2kG_2J_2 + J_4\phi_2)$; $J_{15} = (-2kG_2h_1J_1 + h_2J_3\phi_2)$; $J_{16} = (-2kG_2h_1J_2 + h_2J_4\phi_2)$; $\phi_1 = \partial\pi_1/\partial h_1 - \partial\pi_2/\partial h_1$; $\phi_2 = \partial\pi_1/\partial h_2 - \partial\pi_2/\partial h_2$; and $\phi_3 = \partial\pi_2/\partial h_1$; and $\phi_4 = \partial\pi_2/\partial h_2$.